Modeling of atmospheric-pressure plasma columns sustained by surface waves

Y. Kabouzi* and D. B. Graves†
Department of Chemical Engineering, University of California, Berkeley, California 94720, USA

E. Castaños-Martínez and M. Moisan‡
Groupe de Physique des Plasmas, Université de Montréal, Montréal, Canada H3C 3J7
(Received 27 September 2006; published 9 January 2007)

A self-consistent two-dimensional fluid-plasma model coupled to Maxwell's equations is presented for argon discharges sustained at atmospheric pressure by the propagation of an electromagnetic surface wave. The numerical simulation provides the full axial and radial structure of the surface-wave plasma column and the distribution of the electromagnetic fields for given discharge operating conditions. To describe the contraction phenomenon, a characteristic feature of high-pressure discharges, we consider the kinetics of argon molecular ions in the charged-particle balance. An original feature of the model is to take into account the gas flow by solving self-consistently the mass, momentum, and energy balance equations for neutral particles. Accounting for the gas flow explains reported discrepancies between measured and calculated plasma parameters when assuming the local axial uniformity approximation. In contrast to the low-pressure case, the latter approximation is shown to be of limited validity at atmospheric pressure. The gas temperature is found to be a key parameter in modeling surface-wave discharges sustained at atmospheric pressure. It determines the radial and the axial structure of the plasma column. The calculated plasma parameters and wave propagation characteristics using the present two-dimensional fluid model are in good agreement with our set of experimental data.

DOI: 10.1103/PhysRevE.75.016402 PACS number(s): 52.80.Pi, 52.20.Fs, 52.20.Hv, 52.25.−b

I. INTRODUCTION

It is well known that electromagnetic surface waves can efficiently produce and sustain long plasma columns. It is the most common plasma source based on traveling waves [1]. The surface wave uses the interface between the plasma and the surrounding dielectrics (discharge tube+air) as its propagating medium. The produced plasma column thereby constitutes an essential part of the waveguiding structure: the wave and plasma properties are interdependent. Surface-wave discharges (SWDs) can be sustained over a range of pressure extending from few mtorr to several atmospheres and over the radio-frequency and microwave frequency domains (1 MHz–40 GHz). As far as the discharge vessel is concerned, SWDs can be sustained in cylindrical tubular reactor or in "flat" configuration (e.g., large areas suitable for material processing). Over the past 20 years, surface-wave discharges have attracted increasing interest in the scientific community and are currently utilized in several technological applications. A review of surface-wave discharge properties and applications can be found in Refs. [2–5].

The properties of surface-wave sustained plasma columns have been extensively studied both theoretically and experimentally. Among the existing types of high-frequency (hf) discharges [41], the modeling of SWDs is most advanced at reduced pressure (0.1–10 torr) [6]. At higher pressures, the modeling of SWDs remained, until recently, limited mainly because of the difficulty to account for complex phenomena governing the discharge properties such as its radial contraction and filamentation [7,8]. In a previous publication [9], a self-consistent model for an argon SWD sustained at atmospheric pressure was developed and the basic physical processes governing this discharge were discussed. The onset of radial contraction was shown to depend only on radially nonuniform gas heating. The latter induces contraction through its influence on the kinetics of rare-gas molecular ions, which controls the charged-particle balance. Recently, collisional-radiative models have been developed for such high-pressure argon discharges [10,11]. These studies emphasized the key role played by rare-gas molecular ions in the discharge maintenance processes and particularly their strong influence on the charged-particle balance.

Because the plasma column in SWDs is radially and axially nonuniform, a complete description of these discharges requires a simultaneous and self-consistent solution of Maxwell's equations along with a set of fluid-plasma equations. Due to the strong coupling between the wave and the plasma, this analysis is numerically laborious, even in the simplest situation. A common approach used to simplify this problem is to consider each plasma slab delimited by the axial planes z and $z+\Delta z$ to be axially uniform by assuming the axial gradient of any quantity to be *locally* negligibly small as compared to its corresponding radial gradient [12,13]. Under this uniformity approximation, the analysis of SWDs can be performed in two stages. In a first stage, the radial distribution of the plasma parameters and the values of the wave propagation characteristics are obtained from the plasma maintenance equations and the wave-field equation, respectively, for given discharge operating conditions and power $L(z)$ delivered, per unit length at the axial position z, from the wave-field to the plasma. Therefore, for given discharge

*Present address: Groupe de Physique des Plasmas, Département de Physique, Université de Montréal, Montréal, Canada H3C 3J7; Electronic address: yassine.kabouzi@umontreal.ca
†Electronic address: graves@berkeley.edu
‡Electronic address: michel.moisan@umontreal.ca

operating conditions, the plasma parameters and the wave propagation characteristics are, at any axial position z, only functions of the power per unit length $L(z)$ absorbed at the same axial position z. Then, once the attenuation characteristic $\alpha(L)$ is obtained from the first stage of the analysis, the axial distribution $L(z)$ of the power density can be determined from the wave energy balance equation, in a second stage [14]. Finally, merging the results from the radial distributions of any plasma parameter for given set of values of L with the axial distribution of $L(z)$ enables one to determine the full spatial distribution of this parameter.

The above local axial uniformity approximation (LAUA) has been widely used in modeling both low- and atmospheric-pressure SWDs [13–15]. Although the agreement between measured and calculated plasma parameters and wave propagation characteristics were found to be satisfactory at low pressure, some studies reported discrepancies between theory and experiments at atmospheric pressure [9,15]. In this paper, we adopt an alternative approach that calls for a numerical solution of the full Maxwell's equations coupled self-consistently to a set of fluid-plasma equations. A similar approach has been developed recently by several authors to study SWDs sustained at low pressure [16–19]. The analysis that we have chosen here follows from the fact that, in a contracted discharge sustained at atmospheric pressure, the discharge processes depend nonlinearly on the plasma parameters. For instance, a small change in the gas temperature can induce large variations in the electron density [9], which in turn may affect the wave propagation characteristics. Therefore, the influence of axial nonuniformities in the plasma parameters on the discharge properties cannot be neglected, as is the case under the local axial uniformity approximation. The axial structure of the plasma column not only depends on the wave attenuation characteristic $\alpha(L)$ but also on the specific spatial distribution of each plasma parameter such as the gas temperature distribution, which is partly imposed by the gas flow.

The main purpose of the present work is to investigate the properties of SWDs sustained at atmospheric pressure using a two-dimensional (2D) fluid-plasma model coupled, self-consistently, to Maxwell's equations. To describe the physical processes governing the discharge and to determine the properties of the plasma column, we turn to our previous collisional model for argon discharges [9]. This model considers argon atoms in the ground state, in the metastable states (the first excited configuration taken as a block and further designated 4*s* block) and in the first ionized state. The kinetics of argon atoms is coupled to that of argon molecular ions through the processes of ion-conversion, dissociative recombination and electron- and atom-impact dissociation of molecular ions. Although simplified, this kinetic scheme provides the main characteristics of the ionization-recombination processes governing these atmospheric-pressure discharges. Moreover, the local axial uniformity approximation is not assumed *a priori*, enabling us to determine the effects of the gas flow on the discharge properties and wave propagation characteristics. To the authors' knowledge, it is the first time that such a coupling between the gas flow, the plasma parameters and the surface wave propagation characteristics is treated self-consistently.

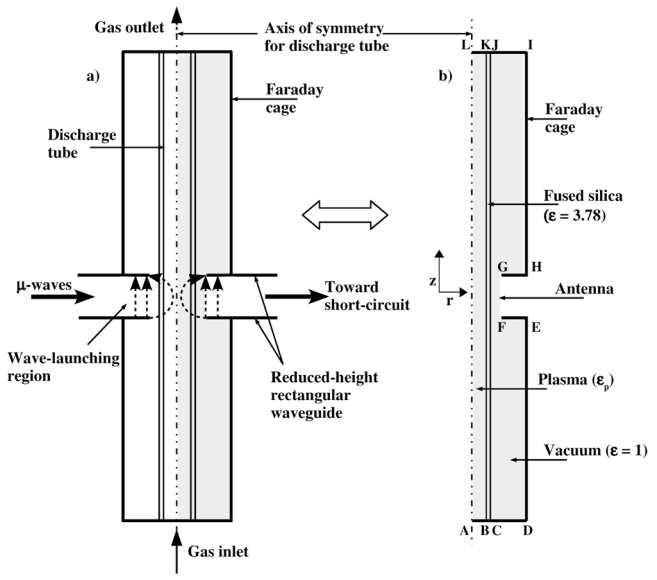

FIG. 1. Schematic representation of the (a) surface-wave plasma source and (b) computational domain. The wave-launching region is modeled by an antenna condition, where the intensity of the axial component of the electric field is set to an arbitrary reference value. The dashed-line arrows indicate the direction of the electric field in the vicinity of the launching gap region.

The paper is organized as follows. Section II presents the equations describing argon SWDs sustained at atmospheric pressure as well as the procedure for solving the resulting set of partial differential equations. In Sec. III, we present the results of our model and discuss the influence of the gas flow rate on the properties of SWDs. Also, we compare the model predictions to our set of experimental data and to previously presented results stemming from a model based on the LAUA. Finally, concluding remarks are provided in Sec. IV.

II. SURFACE-WAVE DISCHARGE MODEL

We consider an argon-plasma column with length much greater than radius, sustained by an azimuthally symmetric surface wave at the frequency of 915 MHz. The microwave discharge is sustained in a dielectric tube with internal and external radii $R=3$ mm and $R_1=4$ mm, respectively. The discharge tube is 60–80 cm long, depending on the power used. The dielectric tube is surrounded by a cylindrical metallic conducting sleeve [see Fig. 1(a)], forming a Faraday cage that confines the electromagnetic fields within the field-applicator region. The diameter of this Faraday cage is 3 cm such that it operates at the cutoff at the frequency of 915 MHz. The surface wave is excited by a surfaguide field applicator (see Fig. 2). Although details of the field applicator are not taken into account when computing the electromagnetic fields, we have considered in the simulation the wave-launching region of the surfaguide (see Figs. 1 and 2), which is delimited by two circular holes pierced in the center of the reduced height section of the waveguide, surrounding coaxially the discharge tube. Figures 1(a) and 1(b) show

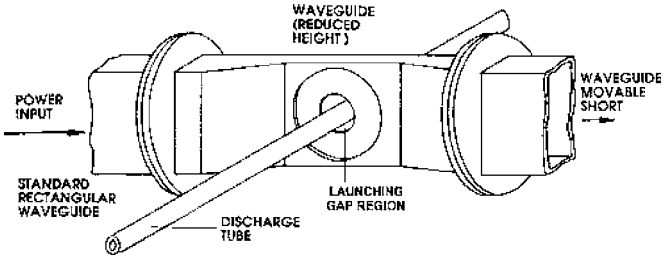

FIG. 2. The surfaguide field applicator and the discharge tube. After Ref. [3], Chap. 3.

schematically the surface-wave plasma source and the computational domain, respectively. The wave-launching region is modeled using an antenna condition, where the intensity of the axial field component is set to an arbitrary reference value. The argon gas flows from bottom to top of the discharge tube [as shown in Fig. 1(a)], and the gas pressure at the exhaust is set to atmospheric pressure ($1.013\,25 \times 10^5$ Pa).

A. Plasma equations

The fluid plasma is considered to be formed by two main species, the electrons and the heavy particles. The electrons are characterized by a Maxwellian energy distribution function with a temperature T_e. The heavy particles comprise argon atoms in the ground state and in metastable states ($4s$ block), argon atomic ions (AIs) and argon molecular ions (MIs). These heavy particles are assumed to be in thermal equilibrium at a temperature T_g (the gas temperature), where $T_g \ll T_e$.

The densities of charged particles are obtained from a set of particle-balance equations assuming the quasineutrality of the plasma [20]. For each ionic species, we calculate its density from a continuity equation of the form,

$$\nabla \cdot (-D_i \nabla n_i + n_i \mathbf{u}) = S_i^i(n_e, T_e, T_g) - S_i^r(n_e, T_e, T_g), \quad (1)$$

where $\mathbf{u}$, n_e, n_i, D_i, S_i^i, and S_i^r are the mass-average velocity (see further below), the electron density, the density of atomic ($i=1$) or molecular ($i=2$) ions, the ambipolar diffusion coefficient, the creation and loss terms for the ionic species, respectively. The latter creation and loss terms are sensitive functions of n_e, T_e, and T_g [9]. The electron density and flux are determined from the conditions for quasineutrality and charge conservation, respectively,

$$n_e = n_1 + n_2, \quad (2)$$

$$\mathbf{\Gamma_e} = -\nabla \cdot (D_1 \nabla n_1) - \nabla \cdot (D_2 \nabla n_2) + n_e \mathbf{u}, \quad (3)$$

where $\mathbf{\Gamma_e}$ is the electron flux. The collisional processes considered in this study and the expression of their rate coefficients are summarized in Table I.

The electron temperature T_e is determined from the electron energy balance equation,

$$\nabla \cdot \left(\tfrac{5}{2} k_B T_e \mathbf{\Gamma_e} - \lambda_e \nabla T_e\right) = \sigma E_0^2 |\mathbf{E}|^2 - \tfrac{3}{2} \delta_{\mathrm{Ar}} k_B \nu n_e (T_e - T_g) - \tfrac{3}{2} n_e \nu^* U^*, \quad (4)$$

where σ is the real part of the plasma electric conductivity, $|\mathbf{E}|$ is the total electric field intensity, E_0 is a normalization constant [see Eq. (14) below], ν is the frequency of elastic collisions for momentum transfer, ν^* is the frequency of inelastic collisions for total excitation [23], U^* is the energy of the first excited state of argon ($U^*=11.548$ eV), k_B is the Boltzmann constant, $\delta_{\mathrm{Ar}}=2m_e/M$ (where m_e and M are the electron and atom masses, respectively) is the energy transfer coefficient for elastic collisions, and λ_e is the electron thermal conductivity.

To account for the neutral gas flow, we need to solve the mass, momentum and energy balance equations determining the mass density, the mass-average velocity and the gas temperature, respectively. The mass continuity equation reads

$$\nabla \cdot (\rho \mathbf{u}) = 0, \quad (5)$$

where the total mass density ρ is given by

$$\rho = NM + n_e(M + m_e) \approx (N + n_e)M, \quad (6)$$

where N is the atom number density, which is determined from Dalton's law,

$$N = \frac{p}{k_b T_g} - n_e\left(1 + \frac{T_e}{T_g}\right), \quad (7)$$

where p is the gas pressure.

The momentum balance equation reads

$$\rho(\mathbf{u} \cdot \nabla)\mathbf{u} = -\nabla p - \nabla \cdot \overleftrightarrow{\tau}, \quad (8)$$

and the gas energy balance equation is

$$\rho C_p (\mathbf{u} \cdot \nabla) T_g = \nabla \cdot (\lambda_g \nabla T_g) - p \nabla \cdot \mathbf{u} + \tfrac{3}{2} \delta_{\mathrm{Ar}} k_B \nu n_e (T_e - T_g), \quad (9)$$

where C_p is the heat capacity at constant pressure, λ_g is the gas thermal conductivity, and $\overleftrightarrow{\tau}$ is the viscous stress tensor for a Newtonian fluid.

B. Wave-field equations

In this model, the plasma column is sustained by an azimuthally symmetric surface wave propagating in a transverse magnetic (TM) mode, where the nonzero wave-field components are E_r, E_z, and H_ϕ. Assuming a harmonic time variation for the wave-field components ($\mathbf{E}$, $\mathbf{H} \sim e^{i\omega t}$, where ω is the wave angular frequency), one can readily derive from Maxwell's equations the wave-field equation for the magnetic field component. In cylindrical coordinates, this equation can be written as

$$\frac{\partial}{\partial r}\left(\epsilon_r^{-1} \frac{1}{r} \frac{\partial (r H_\phi)}{\partial r}\right) + \frac{\partial}{\partial z}\left(\epsilon_r^{-1} \frac{\partial H_\phi}{\partial z}\right) + k_0 H_\phi = 0, \quad (10)$$

where $k_0=\omega/c$ is the free-space wave number, c being the velocity of light in vacuum, and ϵ_r the relative permittivity of the medium. In the plasma, the permittivity is expressed as

TABLE I. List of elementary processes taken into account in the collisional model for argon discharges at atmospheric pressure.

Description	Reaction	Rate coefficient/frequency	Refs.
Elastic scattering	$e+M \rightarrow e+M$ $M=\mathrm{Ar}, \mathrm{Ar}^+, \mathrm{Ar}_2^+$	$\nu=\nu_{en}+\nu_{ei}$ $\nu_{en}(\mathrm{s}^{-1})=1.84\times10^{-8}T_e^{3/2}(\mathrm{eV})$ $\nu_{ei}(\mathrm{s}^{-1})=\frac{4.8n_e(\mathrm{cm}^{-3})}{T_e^{3/2}(\mathrm{K})}\ln\left(\frac{T_e^{3/2}(\mathrm{K})}{1.21\times\sqrt{[n_e(\mathrm{cm}^{-3})]}}\right)$	[21,22]
Excitation	$\mathrm{Ar}+e \rightarrow \mathrm{Ar}(4s)+e$	$k_{0j}(\mathrm{cm}^3\,\mathrm{s}^{-1})=4.9\times10^{-9}T_e^{1/2}(\mathrm{eV})\exp\left(\frac{-11.65}{T_e(\mathrm{eV})}\right)$	[23]
Dexcitation	$\mathrm{Ar}(4s)+e \rightarrow \mathrm{Ar}+e$	$k_{j0}(\mathrm{cm}^3\,\mathrm{s}^{-1})=4.8\times10^{-10}T_e^{1/2}(\mathrm{eV})$	[23]
Ionization	$\mathrm{Ar}+e \rightarrow \mathrm{Ar}^+ +2e$	$k_{0i}(\mathrm{cm}^3\,\mathrm{s}^{-1})=1.27\times10^{-8}T_e^{1/2}(\mathrm{eV})\exp\left(\frac{-15.76}{T_e(\mathrm{eV})}\right)$	[23]
	$\mathrm{Ar}(4s)+e \rightarrow \mathrm{Ar}^+ +2e$	$k_{ji}(\mathrm{cm}^3\,\mathrm{s}^{-1})=1.37\times10^{-7}T_e^{1/2}(\mathrm{eV})\exp\left(\frac{-4.11}{T_e(\mathrm{eV})}\right)$	[23]
Three-body recombination	$\mathrm{Ar}^+ +2e \rightarrow \mathrm{Ar}+e$	$\rho_{tr}(\mathrm{cm}^6\,\mathrm{s}^{-1})=8.75\times10^{-27}T_e^{-9/4}(\mathrm{eV})$	[24]
Dissociative recombination	$\mathrm{Ar}_2^+ +e \rightarrow \mathrm{Ar}(4s)+\mathrm{Ar}$	$\rho_{dr}(\mathrm{cm}^3\,\mathrm{s}^{-1})=1.04\times10^{-6}[T_e(\mathrm{K})/300]^{-0.67}\times\frac{1-\exp[-418/T_g(\mathrm{K})]}{1-0.31\exp[-418/T_g(\mathrm{K})]}$	[25]
Diffusion	$M \rightarrow \mathrm{wall}$ $M=\mathrm{Ar}(4s), e, \mathrm{Ar}^+, \mathrm{Ar}_2^+$		[22,26]
AIs conversion	$\mathrm{Ar}^+ +2\mathrm{Ar} \rightarrow \mathrm{Ar}_2^+ +\mathrm{Ar}$	$k_1(\mathrm{cm}^6\,\mathrm{s}^{-1})=2.25\times10^{-31}[T_g(\mathrm{K})/300]^{-0.4}$	[27]
MIs dissociation			
Electron impact	$\mathrm{Ar}_2^+ +e \rightarrow \mathrm{Ar}^+ +\mathrm{Ar}+e$	$k_2(\mathrm{cm}^3\,\mathrm{s}^{-1})=1.11\times10^{-6}\exp\left(-\frac{2.94-3[T_g(\mathrm{eV})-0.026]}{T_e(\mathrm{eV})}\right)$	[28]
Atom impact	$\mathrm{Ar}_2^+ +\mathrm{Ar} \rightarrow \mathrm{Ar}^+ +2\mathrm{Ar}$	$k_3(\mathrm{cm}^3\,\mathrm{s}^{-1})=\frac{5.22\times10^{-10}}{T_g(\mathrm{eV})}\exp\left(-\frac{1.304}{T_g(\mathrm{eV})}\right)$	[28]

$$\epsilon_p = 1 - \frac{\left(\frac{\omega_p}{\omega}\right)^2}{1 - j\frac{\nu}{\omega}}, \tag{11}$$

where $\omega_p=\sqrt{\frac{e^2 n_e}{m_e \epsilon_0}}$ (e and ϵ_0 are the elementary charge and the permittivity of vacuum, respectively) is the plasma angular frequency.

The radial and axial components of the electric field are then obtained from Maxwell's equations,

$$\frac{\partial H_\phi}{\partial z} = -j\omega\epsilon_0\epsilon_r E_r, \tag{12}$$

$$\frac{1}{r}\frac{\partial (rH_\phi)}{\partial r} = j\omega\epsilon_0\epsilon_r E_z. \tag{13}$$

The numerical solution of Eq. (10), together with Eqs. (12) and (13) provide the spatial distributions of the electromagnetic field components everywhere in the computational domain. The microwave power absorbed by the plasma column is obtained by integrating the power density over the discharge volume,

$$P = E_0 \int_0^R 2\pi r dr \int_{-\ell/2}^{\ell/2} dz \sigma |\mathbf{E}|^2, \tag{14}$$

where $|\mathbf{E}|=\sqrt{|E_r|^2+|E_z|^2}$ is the total electric field intensity, ℓ is the discharge tube length, and E_0 is a normalization constant, which is obtained by solving the above integral for a fixed absorbed microwave power P, the value of which is an input parameter in the simulation.

C. Boundary conditions and numerical procedure

Figure 1(b) shows a schematic representation of the computational domains with the different boundaries. The plasma and gas flow equations are solved in the ABKL domain, representing the discharge tube. The computational domain for the electromagnetic fields comprises three zones defined by their relative permittivities [see Fig. 1(b)], namely the plasma, the fused silica tube and vacuum, which is surrounded by a Faraday cage forming a perfect electric conductor.

Equations (1), (4), (5), and (8)–(10) are subjected to appropriate boundary conditions. For the plasma and neutral gas flow equations, the boundary conditions are summarized in Table II. At the gas inlet, the axial velocity is assumed to follow a parabolic profile given by

TABLE II. Boundary conditions for the plasma and gas flow equations used in the simulation [see Fig. 1(b) for boundary description].

	AB	BK	KL	LA
n_i	$\frac{\partial n_i}{\partial z}=0$	$\frac{\partial n_i}{\partial r}=0$	$\frac{\partial n_i}{\partial z}=0$	$\frac{\partial n_i}{\partial r}=0$
T_e	$\frac{\partial T_e}{\partial r}=0$	$\frac{\partial T_e}{\partial r}=0$	$\frac{\partial T_e}{\partial r}=0$	$\frac{\partial T_e}{\partial r}=0$
T_g	700 K	700 K	$\frac{\partial T_g}{\partial z}=0$	$\frac{\partial T_g}{\partial r}=0$
u_r	0	0	0	0
u_z	u_0	0	$\frac{\partial u_z}{\partial z}=0$	$\frac{\partial u_z}{\partial r}=0$

$$u_0 = \frac{2\Phi}{\pi R^2}\left[1-\left(\frac{r}{R}\right)^2\right], \tag{15}$$

where Φ is the gas flow rate and R is the discharge tube inner radius. The boundary conditions for the electromagnetic fields are shown in Table III. The wave launching region is modeled using an antenna condition, where the intensity of the axial component of the electric field is set to unity.

The plasma and wave equations are solved numerically, using finite element methods implemented in the commercial package FEMLAB® [29]. The numerical approach is schematically represented by the flowchart in Fig. 3 and consists of solving iteratively and successively the set of plasma and neutral gas flow equations [Eqs. (1)–(4) and (5)–(9)] along with the wave equation (10), constrained by Eq. (14). The calculations start with an initial guess for the distributions of the plasma parameters $[n_e(r,z), T_e(r,z), T_g(r,z), \mathbf{u}(r,z)]$ and the deposited power density $\sigma|E|^2(r,z)$. In a first step, Eqs. (5)–(9) for the neutral gas flow and Eq. (10) for the wave-field subject to the appropriate boundary conditions are solved until the power balance specified by Eq. (14) is fulfilled. In a second step, the set of plasma equations (1)–(4) and the wave-field equation (10) are solved, using the calculated distributions of T_g, $\mathbf{u}$, and ρ, until the power balance specified by Eq. (14) is fulfilled again. The procedure is repeated until global convergence of all the distributions is achieved. In this case, the normalization constant E_0 determined at each step of the calculations does not vary noticeably (less than 1%). Typically, four to five iterations suffice to achieve global convergence.

Special consideration is needed to avoid singularities in the electrical field components (E_r, E_z) at locations where the electron density is equal to the critical density, and the plasma permittivity crosses zero [30]. From Eq. (11), one can readily obtain the conditions for which $\epsilon_p=0$,

$$\mathrm{Re}\{\epsilon_p\}=0 \quad \text{for } n_e = n_c\left[1+\left(\frac{\nu}{\omega}\right)^2\right], \tag{16}$$

$$\mathrm{Im}\{\epsilon_p\}=0 \quad \text{for } n_e=0, \tag{17}$$

where $\left(n_c=\omega^2\frac{m_e\epsilon_0}{e^2}\right)$ is the critical density. To avoid the singularity, the electron density in Eq. (11) is arbitrarily modified by adding a background density equal to 2 times the value given by Eq. (16). In such a way, the singularities in the field components disappear, but one can still obtain a strong maximum in the field intensity close to the end of the plasma column (see Sec. III A further below).

The above assumption can affect the values of both the real and the imaginary parts of the plasma permittivity. However, the changes to the plasma permittivity resulting from this assumption are found to be less than 10% over most of the plasma column (less than 1% at the discharge axis). Using the LAUA model, we have also checked that neither the wave propagation characteristics nor the plasma parameters are altered by the use of the above assumption.

A comprehensive treatment of the plasma resonance at reduced pressures can be found in Ref. [31], where the sheath-resonance phenomena were taken into account in the local budget of the discharge power deposition. In Ref. [31], a semianalytical solution of the surface-wave field equation [Eq. (10)] in one dimension was used to prevent numerical problems associated with the strong variations in the resonance region of the plasma permittivity and wave-field components. Such an analysis is, however, outside the scope of the present two-dimensional study.

III. RESULTS AND DISCUSSION

The plasma parameters and the surface-wave field components are numerically computed for given absorbed micro-

TABLE III. Boundary conditions for the electromagnetic fields [see Fig. 1(b)].

AC/EF/GH/IL	DE/HI	FG	LA	BK/CJ
PEC[a] $(E_r=0)$	PEC $(E_z=0)$	Antenna $(\lvert E_z\rvert=1)$	Symmetry $(E_r, H_\phi=0)$	Continuity tangential components (E_z, H_ϕ)

[a]Perfect electric conductor.

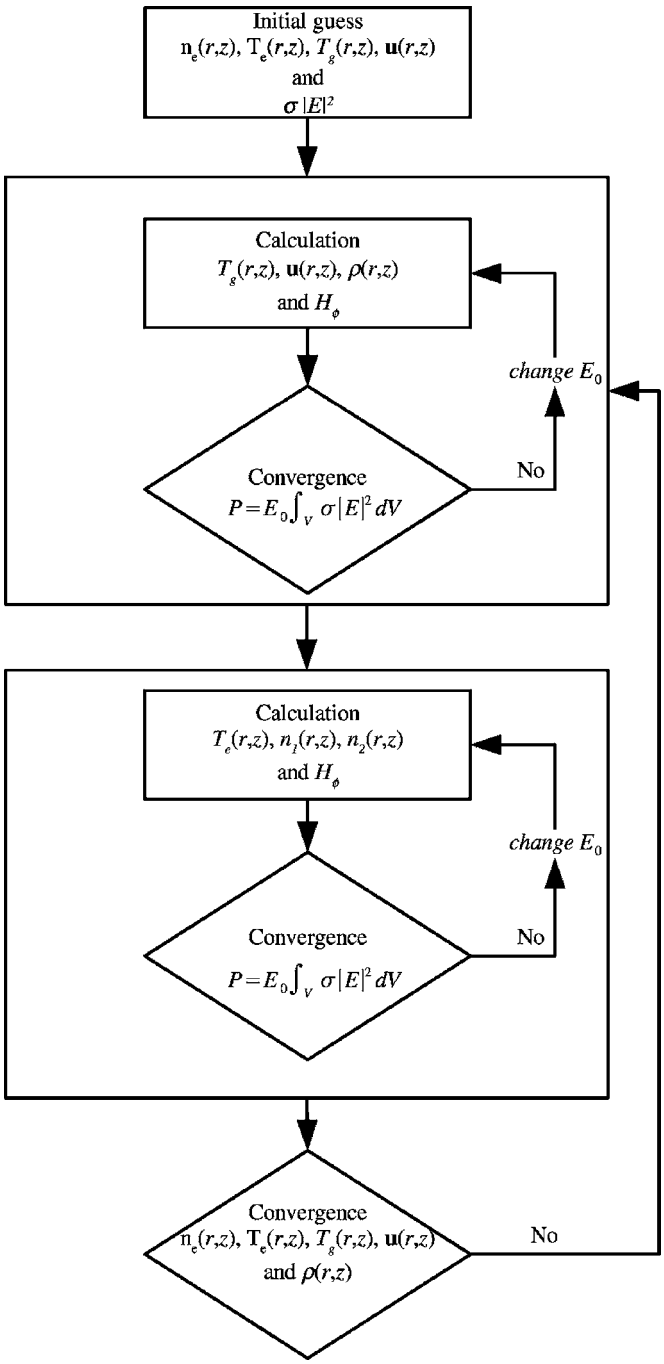

FIG. 3. Flow chart of the numerical calculations.

wave power (P) and gas flow rate (Φ), the only input parameters in the simulation. The discharge tube dimensions, the field frequency and the outlet pressure are fixed in this study. The simulation results are compared with those obtained under the LAUA [9] and with experimental measurements obtained in argon under the same discharge operating conditions.

A. Spatial distribution of plasma parameters and wave-field components

Figures 4(a) and 4(b) show the spatial distributions of the electron density and electron temperature, respectively, for

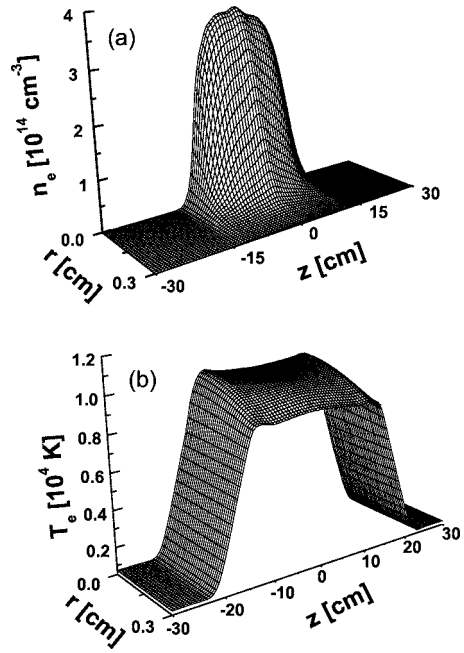

FIG. 4. Distributions of the (a) electron density and (b) electron temperature. $P=150$ W, $\Phi=250$ sccm, $p=1.013\,25\times10^5$ Pa, $f=915$ MHz, $R=3$ mm.

an argon discharge sustained at atmospheric pressure and at $f=915$ MHz. The absorbed microwave power is 150 W and the gas flow rate is 250 sccm (standard cubic centimeter per minute) [42]. The discharge tube radius and length are $R=3$ mm and $\ell=60$ cm, respectively. The gas inlet is located at the axial position $z=-30$ cm, while the gas outlet is located at $z=30$ cm. Both distributions show a symmetric plasma column with respect to the antenna position ($z=0$), which represents the launching gap of the surfaguide (see Fig. 1). Axially, the electron density reaches a maximum at the discharge tube center ($z=0$), where the microwave power is coupled from the antenna to the plasma. The density value there amounts to 3.8×10^{14} cm^{-3}. The density decreases relatively slowly over 7 cm (20% of its peak value) on both sides of the tube center ($z=0$) and then decays almost exponentially toward both ends of the plasma column. Radially, we observe that the plasma column does not fill the discharge tube, i.e., it is contracted. For example, at the tube center ($z=0$), n_e falls off by two orders of magnitude from the axis toward the tube wall as a consequence of the strong gas temperature gradient [see Fig. 5(a)]. Discharge contraction is caused by nonuniform gas heating through its influence on molecular-ion kinetics (see the Appendix and Ref. [9]). Figure 4(b) shows that the electron temperature varies slowly over the discharge cross section and is axially almost uniform, though increasing slightly (from 10 080 K to a maximum value of 10 400 K) toward both ends of the plasma column, where then it decays rapidly.

Figures 5(a) and 5(b) show the spatial distributions of the gas temperature and gas axial velocity, respectively. The spatial profile of the gas temperature is similar to that of the electron density, since elastic collisions are the dominant gas heating mechanism in argon discharges at atmospheric pres-

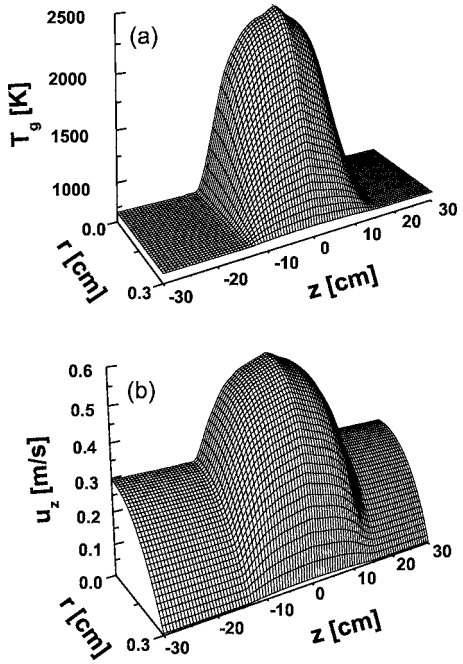

FIG. 5. Distributions of the (a) gas temperature and (b) gas axial velocity. Same conditions as in Fig. 4.

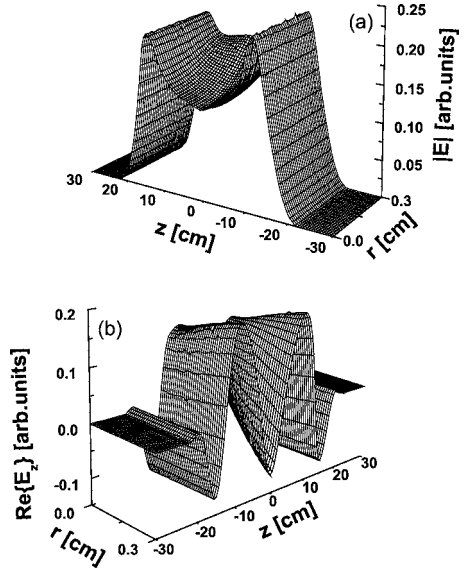

FIG. 6. Spatial distributions of the (a) total electric field intensity and (b) real part of the E_z-field complex amplitude in the plasma. In (b), the phase of the E_z-field component is set to an arbitrary reference value. Same conditions as in Fig. 4.

sure and the only one taken into account in this study. Axially, the gas temperature in the plasma region increases rapidly from a centerline ($r=0$) value of 700 K to 2400 K ($z=0$), then decreases downstream to reach its initial value of 700 K at the gas outlet. At a gas flow rate of 250 sccm, the energy transferred to the gas by elastic collisions with electrons is almost entirely dissipated through thermal conduction to the tube wall: energy transport by axial convection is negligible, even though the discharge tube radius is relatively small ($R=3$ mm). Because of gas heating in the plasma, the total mass density decreases and the axial velocity increases accordingly, as can be seen from Fig. 5(b), to maintain conservation of mass flow.

Figures 6(a) and 6(b) show the spatial distributions of the total electric field intensity and of the real part of the E_z-field component (phase variation), respectively, in the plasma medium. Figure 6(a) shows that the electric field intensity is radially nonuniform (the so-called skin effect). The penetration depth of the electric field in the plasma decreases from the column ends toward the discharge center, where the electron density is the highest, because of the increase of the average electron density (over the discharge cross section) and the decrease of ν/ω (as T_g increases). Also, we observe from Fig. 6(a) an enhancement of the electric field intensity in the vicinity of the plasma column ends ($z\approx\pm 12$ cm), where the electron density approaches the value of the critical density $\left(n_c=\omega^2\frac{m_e\epsilon_0}{e^2}\right)$ [30,32]. The position of this field enhancement is shifted axially toward higher density values due to the presence of strong collisions ($\nu/\omega>1$). Past this field enhancement position, a sharp decay of the electric field intensity occurs and no more wave power is available to sustain the plasma. Figure 6(b) shows that the electric field has an oscillatory behavior along the plasma column and that no reflection occurs at either end. It is also clear from Fig. 6(b) that the plasma column is sustained by two waves traveling in opposite directions with respect to the antenna axial position ($z=0$).

Figures 7(a)–7(c) show the radial distributions of both the plasma parameters and the wave-field components at $z=5.4$ cm. Because of the dissociation of molecular ions (MIs) by atom impact, atomic ions (AIs) are the dominant ion species everywhere except close to the tube wall, where the gas temperature is sufficiently low [$T_g\lesssim 1500$ K, see Fig. 7(b)] such that the density of MIs there exceeds the density of AIs. Figure 7(c) shows the radial distribution of the total electric field intensity and the intensity of its radial and axial components in the three media (plasma, dielectric tube, and vacuum). The two vertical lines delimit the spatial extension of the tube wall (1 mm thickness). The electric field intensity is maximum at the interface between the dielectric tube and vacuum, where the radial component of the electric field is dominant. Conversely, the axial field component is the main sustaining field within the plasma. Figures 8(a) and 8(b) show, on a log scale, the variation of the plasma parameters along the discharge axis ($r=0$). Similarly to the radial variation of the charged-particle densities, the density of MIs is lower than that of AIs inside the plasma column except at the axial ends, where again the gas temperature decreases below 1500 K. From Fig. 8(b), we see that the gas temperature is much lower than the electron temperature everywhere along the plasma column, indicating that the plasma is far from (local) thermodynamic equilibrium. The ratio between the electron temperature and the gas temperature decreases (from 12 to 4), however, as n_e increases, i.e., when moving from the plasma column ends toward the tube center ($z=0$).

B. Influence of gas flow on discharge properties

Although the density of MIs is lower than that of AIs, their kinetics controls the overall ionization-recombination

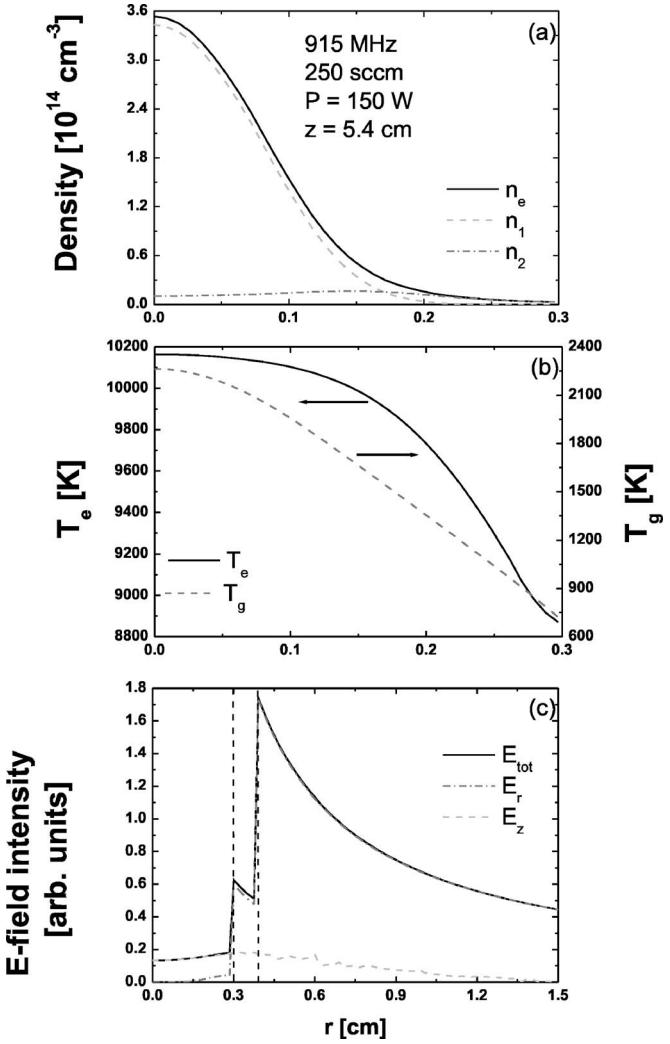

FIG. 7. Radial distributions (at z=5.4 cm) of the (a) charged-particle densities, (b) electron and gas temperatures, and (c) intensity of the electric field components. Note that the radial distance in (c) extends from the tube center to the radial position of the Faraday cage.

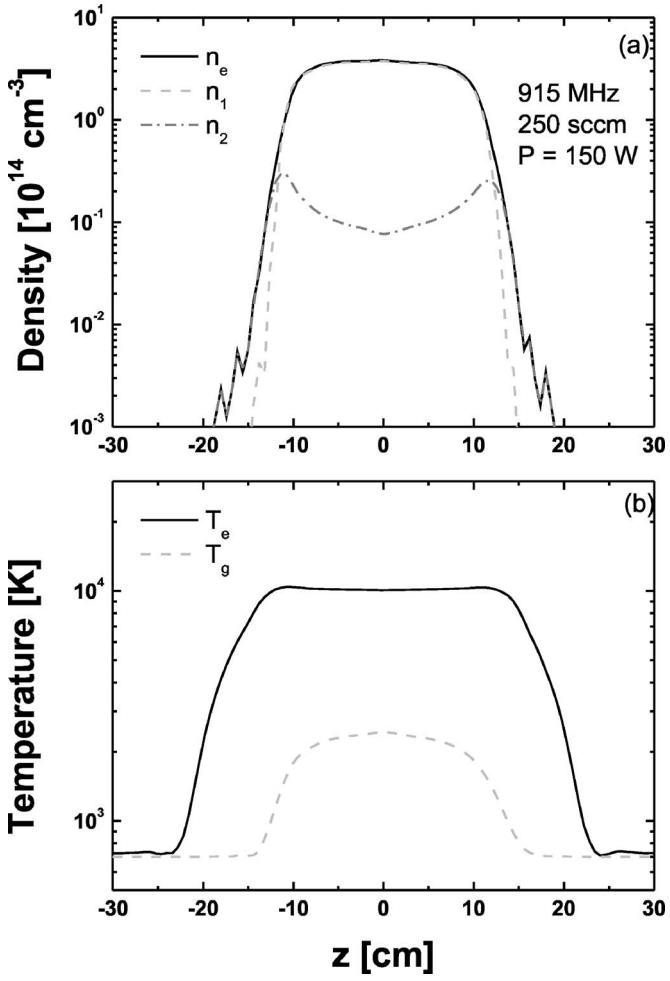

FIG. 8. Axial distributions of the (a) charged-particle densities and (b) electron and gas temperatures along the discharge axis (r =0).

balance of charged particles in argon discharges sustained at atmospheric pressure. Because of atom-impact dissociation of MIs, the electron density depends nonlinearly on the gas temperature (see the Appendix). For instance, the radial gradient of T_g induces a rapid radial decay of n_e, as can be seen in Figs. 4(a) and 7(a). Likewise, the axial gradient of T_g, which depends partly on the gas flow, can affect the electron density axial gradient, influencing thereby the surface-wave propagation characteristics. The influence of the gas temperature on the discharge kinetics and, therefore, on the distribution of the electron density creates an interdependence between the gas flow, the plasma parameters and the wave propagation characteristics in surface-wave plasma columns sustained at atmospheric pressure.

Figures 9(a)–9(c) show the axial distributions of the gas velocity, the gas temperature, and the average electron density (over the discharge cross section), respectively, for different gas flow rates at 150 W. When the gas flow rate is increased from 0.25 to 0.50 slm (standard liter per minute), the axial gas velocity increases in magnitude but nonetheless keeps the same axial profile. The gas temperature is only slightly affected by the increase in the gas flow rate, both in magnitude and profile. The same observations hold for the axial distribution of $\bar{n}_e$. At higher gas flow rates, the gas temperature in the plasma zone increases with its upstream gradient becoming steeper and steeper. As a consequence, the average electron density increases, its gradient becomes steeper and the attenuation of the wave traveling upstream increases (not shown) leading to a shortening of the plasma column upstream [see Fig. 9(c)]. Figure 10 presents the spatial distribution of the electron density in the plasma column for three values of the gas flow rate. Figure 10 shows clearly that at 3 slm, the whole plasma column is shifted axially toward the gas outlet by the convective flow and its length decreases. The SWD at 3 slm looks like the "flame" of a plasma torch, with a well defined zone of high electron density followed by a plume downstream. Moreover, we observe from Fig. 9(b) that the gas temperature at the discharge centerline increases from 2400 K at 0.25 slm to 2700 K at 3 slm, since the power density increases as a result of the reduction of the plasma volume with the gas flow rate. The increase of both T_g and n_e with the gas flow rate has been

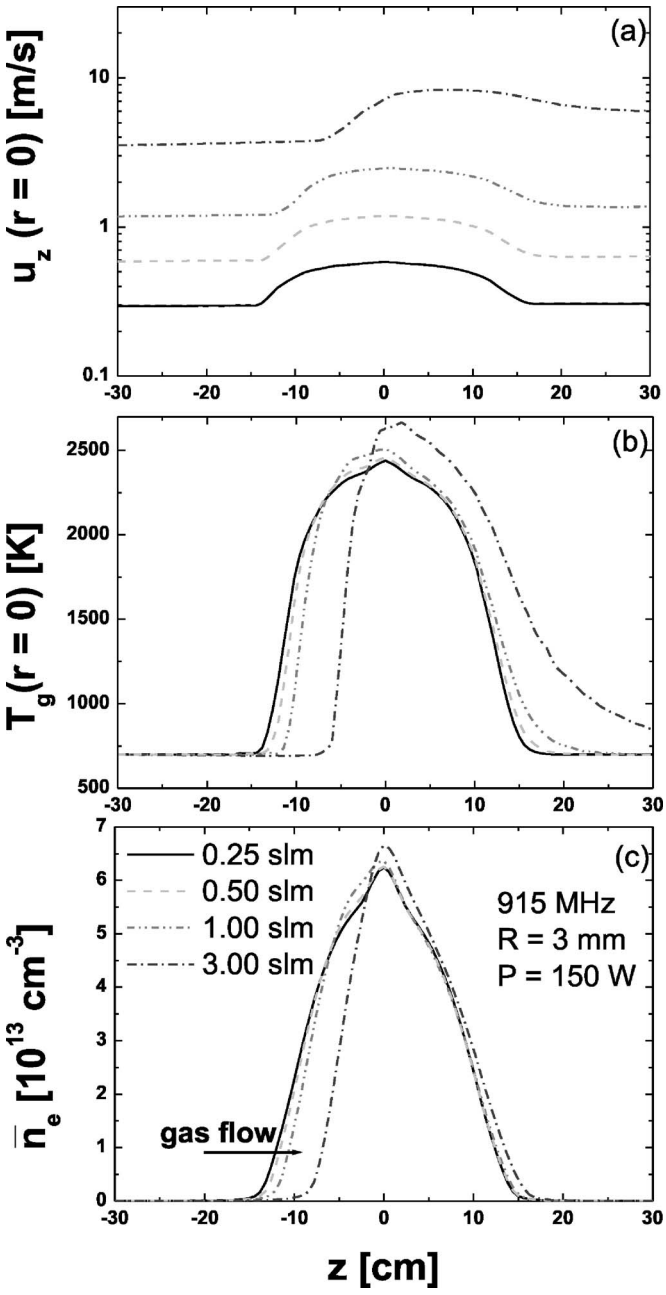

FIG. 9. Axial distributions of (a) the gas velocity, (b) gas temperature, and (c) average electron density, for several gas flow rates at 150 W.

observed experimentally using microwave discharges sustained at atmospheric pressure in nitrogen [33].

Experimentally, we have observed that increasing the gas flow rate leads to a shortening of the plasma column. At high gas flow rate ($\gtrsim$10 slm), the discharge tends to look like the flame of a plasma torch rather than the usual plasma column, indicating that the wave power flux is constrained to travel downstream by the convective flow, in accordance with the above modeling results. Such a coupling between the gas flow, the plasma parameters and the wave propagation characteristics can affect any chemistry occurring in the plasmas. For example, this can adversely affect the abatement of pollutant molecules when using surface-wave plasmas sustained

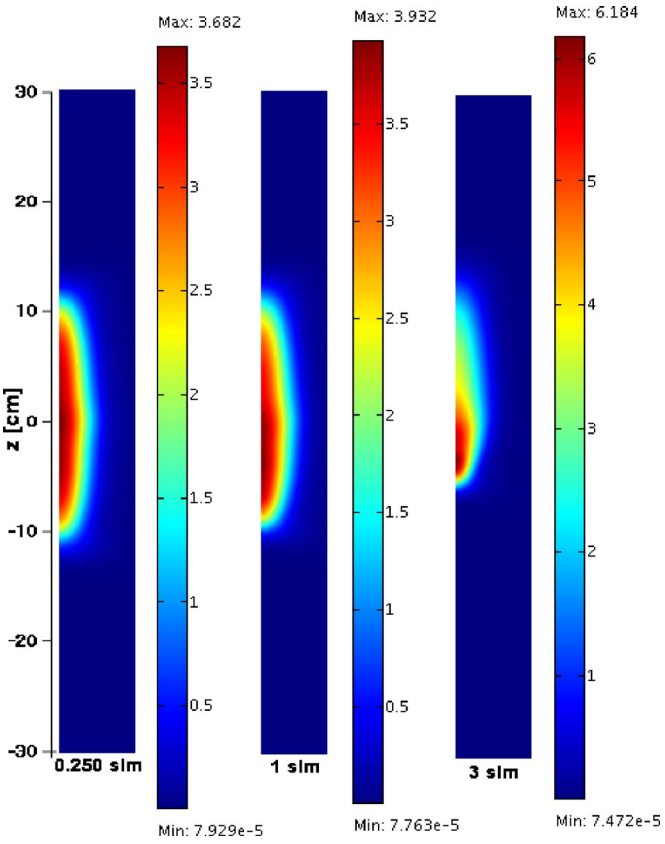

FIG. 10. (Color online) Spatial distribution (r,z) of the electron density ($\times 10^{14}$ cm^{-3}) at 150 W for three gas flow rates.

at atmospheric pressure. At high gas flow rates, the plasma volume shrinks axially while the residence time of molecules to be chemically transformed decreases, resulting in a lowering of the abatement efficiency [34,35].

C. Comparison with experiments and previous modeling results based on the LAUA

The average electron density ($\bar{n}_e$), the plasma column radius (R_p), and the total plasma column length were measured in an argon discharge sustained at atmospheric pressure using optical emission spectroscopy. The electron density was obtained from the Stark broadening of the H_β line (λ =486.13 nm). The procedure for obtaining the average electron density was presented elsewhere [9], but we shall recall it here for the sake of completeness.

Due to the strong radial contraction of the argon discharge, the plasma radius is too small (about 1 mm) to accurately obtain, through Abel inversion, the radial profile of electron density directly from the Stark broadening of the H_β line because of the errors stemming from the Abel inversion procedure. Instead, the average electron density is estimated using the following procedure: (i) the value of the electron density at the discharge axis, $n_e(r=0,z)$, is determined from the Stark broadening of the H_β line, measured along the discharge tube (the emitted light intensity is measured along the line of sight); (ii) the radial profile of n_e is determined from the radial profile of the emitted light intensity of the H_β

$[I_{H_\beta}(r,z)]$ line through Abel inversion, assuming that it reflects the density profile. The average electron density is then obtained at each axial position along the plasma column from the following expression:

$$\bar{n}_e(z) = \frac{n_e(r=0,z)}{\pi R^2} \int_0^R I_{H_\beta}(r,z) 2\pi r dr. \tag{18}$$

The radial profile of the H_β line can deviate from that of the electron density because the hydrogen ground-state density varies along the discharge cross section as a result of the gas temperature gradient. Also, some of the H_β emission may come from dissociative recombination of ArH^+ molecular ions. The average electron density estimated using Eq. (18) is approximately correct since on the one hand, the process of dissociative recombination is believed to be negligible compared to direct excitation of the H_β line through electron impact on hydrogen ground state. On the other hand, the influence of the gas temperature gradient, which varies by a factor of 3 from the discharge axis to the tube wall, on the H_β line is small compared to that of the electron density, which decreases by more than two orders of magnitude over the same distance. Moreover, we have checked experimentally that, under our operating conditions, the radial profile of the H_β emission follows that of the electron density in a neon microwave discharge, for which the plasma radius is relatively large, allowing for an accurate determination of the electron density profile through Abel inversion [36].

The average electron density determined from the model is obtained by integrating the radial distribution of the electron density over the tube cross section

$$\bar{n}_e(z) = \frac{1}{\pi R^2} \int_0^R n_e(r,z) 2\pi r dr. \tag{19}$$

The plasma radius (R_p) is obtained experimentally from the full width at half-maximum (FWHM) of the radial profile of the H_β line, while from the model, R_p is determined from the FWHM of the radial distribution of the electron density. Finally, the plasma column length is inferred from the total emitted light intensity, while from the 2D model, the plasma column length is determined from the axial positions where the total electric field intensity reaches its maximum value [see Fig. 6(a)].

In Fig. 11, we compare the results from the 2D fluid model with our set of experimental data and with results from modeling using the LAUA taken from our previous work [9]. The model results are obtained under the same operating conditions as in experiments, $f=915$ MHz, $R=3$ mm, and $\Phi=250$ sccm (recall that the gas flow is not considered in the model based on the LAUA). The comparison between experiments and models results in Figs. 11(a) and 11(b) are performed for the downstream plasma column only (for axial positions $z>0$ in Fig. 4). The length of this part of the plasma column is noted ℓ_p and its end is chosen as the origin of the z axis for the ease of comparison with experimental results (experimentally, the end of the plasma column is easier to determine than the center position of the field applicator). Figure 11(a) shows that the 2D fluid model predicts well the axial distribution of the electron density,

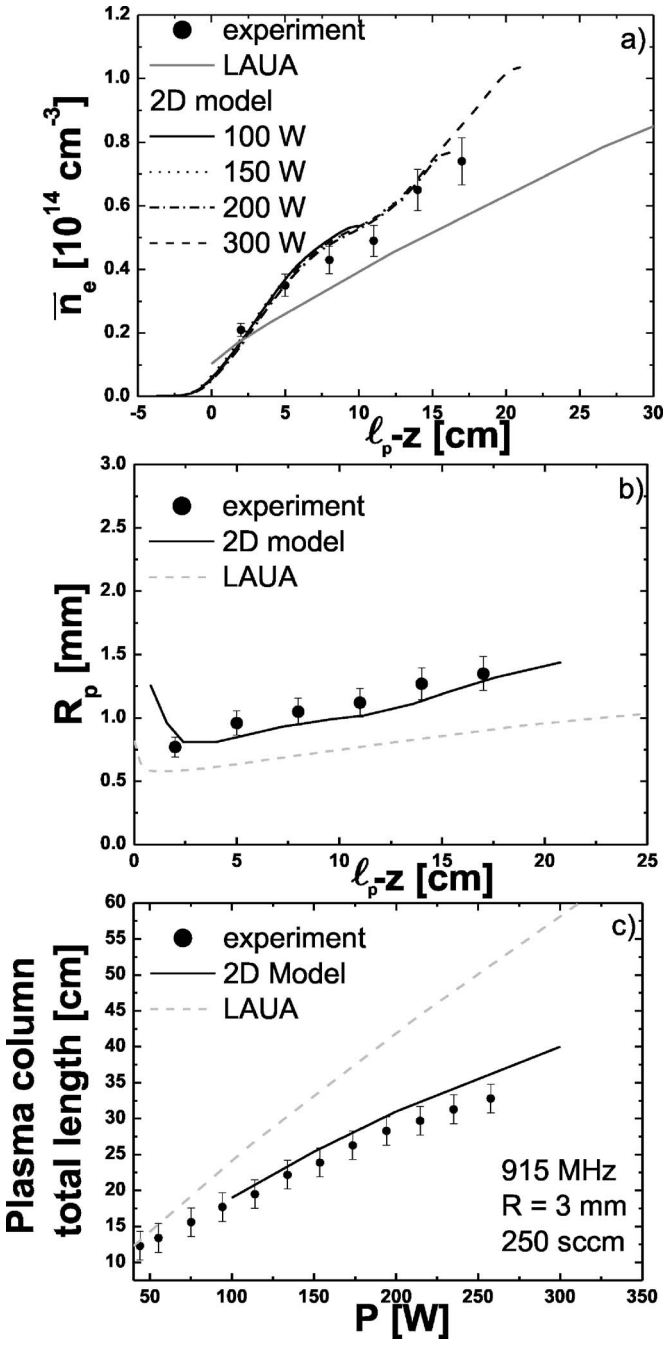

FIG. 11. Comparison between experimental measurements and model predictions (a) average electron density, (b) plasma radius, and (c) plasma column length.

both in magnitude and profile: they differ by 12% at most. We observe that the axial profile of $\bar{n}_e$ is independent of power, i.e., the properties of the plasma column are independent of the wave-launcher position and of our choice of the antenna condition in the model, in accordance with former experiments concerning surface-wave plasmas (SWPs) (Ref. [3], Chap. 5). On the other hand, the model based on the LAUA underestimates by 25% the average electron density along the plasma column. The difference between LAUA results and experiments worsen as the electron density increases. Moreover, both the 2D model results and the experi-

mental data show that $\bar{n}_e$ does not vary linearly along the entire plasma column, in contrast to the LAUA results. We observe that the column is formed by two segments of plasma. A first segment close to the wave launcher ($10 \leqslant \ell_p - z \leqslant 20$ cm for $P=300$ W), where the density increases almost linearly. The extent of this segment of plasma increases with power. A second segment of plasma ($0 \leqslant \ell_p - z \leqslant 10$ cm) representing the end of the column is independent of power. The average electron density decreases rapidly in this last plasma segment.

Figure 11(b) shows that the values of R_p predicted by the 2D fluid model agree well with the experimental measurements. Values of R_p predicted by the model based on the LAUA are lower than the measured ones. However, both models predict an increase of R_p at the very end of the plasma column, which we have observed experimentally with several rare gases. At this axial position, the gas temperature is close to 700 K and MIs are the dominant ionic species. The electron density there amounts to $\sim 10^{12}$ cm^{-3} with an electron temperature of 9000 K. In Fig. 11(c), we compare the calculated and measured plasma column length as a function of the absorbed microwave power. Again, the 2D model predictions are in good agreement with the experimental data, while the model based on the LAUA overestimates the plasma column length.

Figures 12(a) and 12(b) show the calculated axial distributions of the real part of the complex amplitude and the intensity, in dB, of the E_r-field component, respectively, for three microwave power levels, at the interface between the dielectric tube and vacuum. Figure 12(a) shows that the plasma column comprises at least one wavelength (at 100 W): the higher the microwave power, the larger the number of phase maxima and minima appearing along the plasma column. We observe from Fig. 12(b) two distinct regions of wave attenuation along the plasma column. Assuming an axial field variation of the form $\exp(-2\alpha z)$, one notes a region of a slow wave attenuation ($\alpha z \approx$ constant) close to the wave launcher and a region of sharp increase of the wave attenuation toward the end of the column. The latter attenuation region is not modified by the increase of microwave power, while the region of almost constant attenuation extends farther as power is increased. Considering the results in Fig. 11(a), we observe that the region of constant attenuation corresponds to the segment of the plasma column where the density increases linearly, while the region of fast attenuation corresponds to the end segment of the plasma column, for which the density decreases rapidly and its spatial extension is independent of power. Comparing Figs. 12(a) and 12(b) with the experimental results of Moisan *et al.* [37] shown in Figs. 13 and 14, respectively, we observe that the 2D fluid model reproduces qualitatively well the observed experimental features. Note, however, from Fig. 14 that the attenuation of the surface wave is stronger in the experiments than in the 2D model, since the discharge tube radius used in the experiments (noted a in Fig. 14) is smaller than in the 2D model calculations ($R=3$ mm).

D. Validity of the LAUA

Figure 15 shows the calculated wave propagation characteristics along the plasma column, as inferred from the 2D model and from the model based on the LAUA. In the latter case, the end of the plasma column, $z=\ell_p$, is chosen such that the wave attenuation coefficient, α, equals the wave propagation coefficient, β. In the 2D model, the various field components do not have the same attenuation and propagation coefficients [38]. Therefore, the end of the plasma column does not *a priori* occur at the axial position where $\alpha = \beta$. The end of the plasma column is determined, in this case, from the axial position where $|\mathbf{E}|$ reaches it maximum value, as in Figs. 11(a) and 11(b). Figure 15 shows that α is underestimated by the LAUA compared to the 2D model calculations, particularly toward the end of the plasma column where α increases almost exponentially in the 2D model in accordance with the results of Fig. 11(a) and Fig. 12(b). The same remarks hold for the calculated β values from the two models. We observe from the results of the 2D model that β varies monotonically along the plasma column, while the LAUA predicts an almost constant variation of β. The discrepancy between the calculated wave propagation coefficients, however, is not as important as for α. This may be attributable to the smoothing effects of the two media (di-

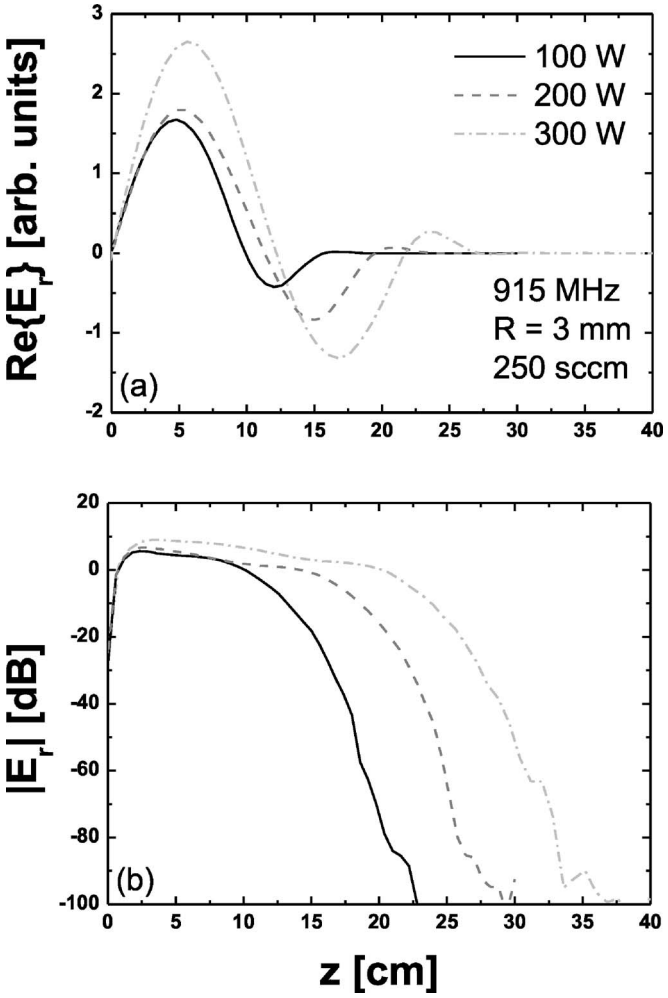

FIG. 12. Calculated axial distributions of the (a) real part of the E_r-field amplitude and (b) E_r-field intensity, for three microwave power levels at the interface between the dielectric tube and vacuum.

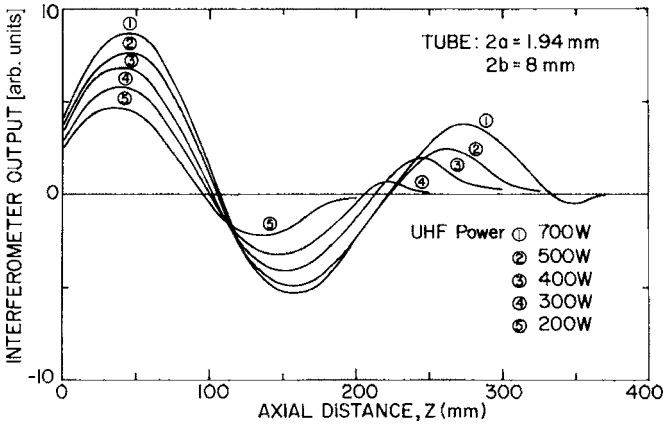

FIG. 13. Recorded surface wave interferograms along the plasma column at the interface between the dielectric tube and vacuum, at various absorbed microwave power in argon discharge sustained at atmospheric pressure and at 915 MHz. The discharge tube inner (a) and outer (b) radii are 0.96 and 4 mm, respectively. After Moisan *et al.* [37].

electric tube+vacuum) surrounding the plasma column and having uniform dielectric permittivities as discussed in Ref. [39].

The above results show that the assumption of the LAUA leads to discrepancies with the experimental measurements in the case of SWPs sustained at atmospheric pressure. For example, the model based on the LAUA predicts slow variations of both the average electron density and the wave attenuation coefficient along the plasma column, while experimental data as well as the 2D model results show a much steeper axial gradient for $\bar{n}_e$ and a stronger wave attenuation. At low gas pressure, although the discharge is axially nonuniform the plasma properties vary slowly along the column. The assumption of the LAUA is then sound, because the variations of the electron density are small in magnitude (typically less than $15n_c$ in most cases) and take place over several wavelengths. At atmospheric pressure, in contrast, the plasma column may only comprise one wavelength over which the electron density can vary by several orders of

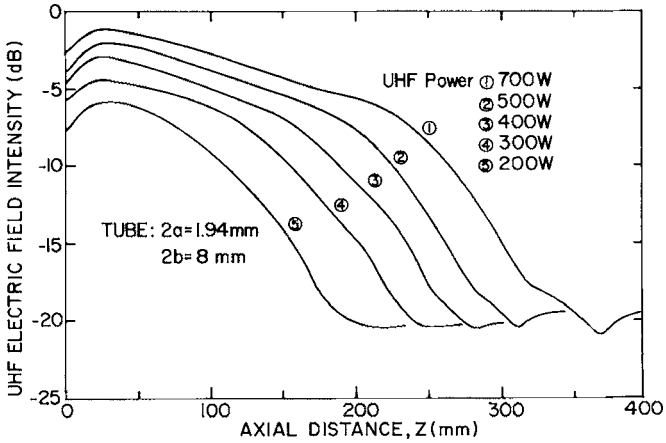

FIG. 14. Recorded axial distributions of the electric field intensity at various absorbed microwave power (same operating conditions as in Fig. 13). After Moisan *et al.* [37].

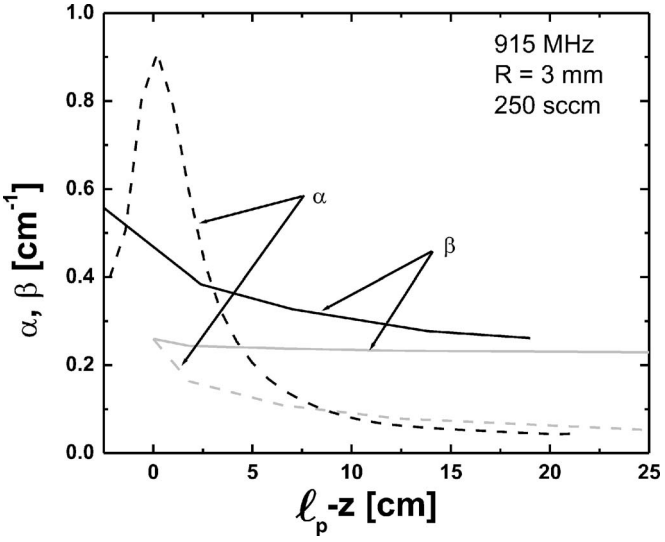

FIG. 15. Calculated attenuation and propagation coefficients using 2D model (black curves) and model based on LAUA (light gray curves).

magnitude. Therefore, even though the plasma column length is much longer than the discharge tube radius [15], the LAUA may fail in predicting accurately SWP properties.

The large axial variation of the electron density observed at atmospheric pressure is mainly due to the nonlinear dependence of charged-particle densities on the gas temperature through its influence on the kinetics of MIs (see the Appendix). The influence of the nonuniform axial variation of the gas temperature on charged-particle densities is particularly strong at the end of the plasma column, where T_g decreases below $\approx$1500 K. There, n_e falls off by more than two orders of magnitude [see Figs. 8(a) and 8(b)], thus inducing a rapid attenuation of the wave, as seen in Fig. 15. Also, because of this axial gradient of T_g, the density of AIs at the end of the plasma column decays by more than four orders of magnitude, while the density of MIs increases to become the dominant ionic species, emphasizing the key role played by molecular ions in the discharge maintenance processes. The above results point out the fact that the knowledge of the attenuation characteristic $\alpha(L)$ by itself does not suffice to determine the full axial structure of SWPs sustained at atmospheric pressure, in contrast with the reduced-pressure case. A more accurate physical description of such traveling wave discharges requires the inclusion of the effects of axial nonuniformities in the discharge maintenance processes and accounting for the gas flow.

IV. CONCLUSION

We have presented a self-consistent two-dimensional model for argon discharges sustained at atmospheric pressure by the propagation of electromagnetic surface waves at microwave frequencies. The model couples Maxwell's equations to a set of fluid-plasma equations, describing the discharge maintenance processes specific to argon discharges. The influence of the gas flow on SWD properties has been, for the first time, taken into account by solving self-

consistently the mass, momentum and energy balance equations for neutral species.

The model emphasizes the key role played by argon molecular ions in the discharge maintenance processes. Taking into account the kinetics of molecular ions enabled us to accurately describe both the radial and the axial structure of SWDs. The spatial structure of the SWD is found to be fully determined by the gas temperature through its influence on the kinetics of molecular ions, the density of which is determined by the local value of the gas temperature. Therefore, the influence of the gas flow (through T_g) on SWD properties derives naturally from this model and is physically meaningful. The gas flow was also shown to affect the propagation characteristics of the surface wave. At high flow rate, the wave space damping rate along the direction opposite to the gas flow can be strong [see Fig. 9(c)]. As a result, the discharge volume decreases, while the gas temperature and the electron density increases. Because of the interdependence between the gas flow, the discharge maintenance processes and the surface-wave propagation characteristics at the local axial uniformity approximation, which has been widely used to model SWDs, is found to be of limited validity at atmospheric pressure.

Model results were compared with experimental measurements obtained with surface-wave discharges sustained in argon at atmospheric pressure, showing good agreement with both the plasma parameters and the wave propagation characteristics.

ACKNOWLEDGMENTS

One of the authors (Y.K.) wishes to acknowledge the support and encouragement of Dr. J.-C. Rostaing (Air Liquide, France) and is indebted to Dr. M. A. Nierode for his help with FEMLAB modeling. This work was supported financially by the Fonds Québcois pour la Recherche sur la Nature et la Technologie (FQRNT) of the Gouvernement du Québec and the Conseil de Recherches en Sciences Naturelles et en Génie (CRSNG) of Canada.

APPENDIX: ROLE OF MOLECULAR-ION KINETICS AND GAS TEMPERATURE IN THE DISCHARGE CONTRACTION

As gas pressure is increased ($p \geqslant 10$ torr in argon discharges), volume dissociative recombination becomes dominant over ambipolar diffusion. In rare-gas discharges, however, dissociative recombination can also affect the charged-particle creation since one of the two atoms resulting from this recombination is in a metastable state, thus enhancing the process of step ionization. More specifically, the kinetics of MIs controls the ionization-recombination balance of charged particles in argon discharges sustained at atmospheric pressure (Ref. [40], Chap. 4). To show this, consider the continuity equation for electrons, which can be written in this case as [9]

$$-\nabla \cdot (D_{ae} \nabla n_e) = \nu_i n_e + \frac{k_{si1} n_e^2 + k_{si2} n_e^2 n_2}{1 + \eta n_e} - \rho_{dr} n_e n_2 - \rho_{tr} n_e^2 n_1. \tag{A1}$$

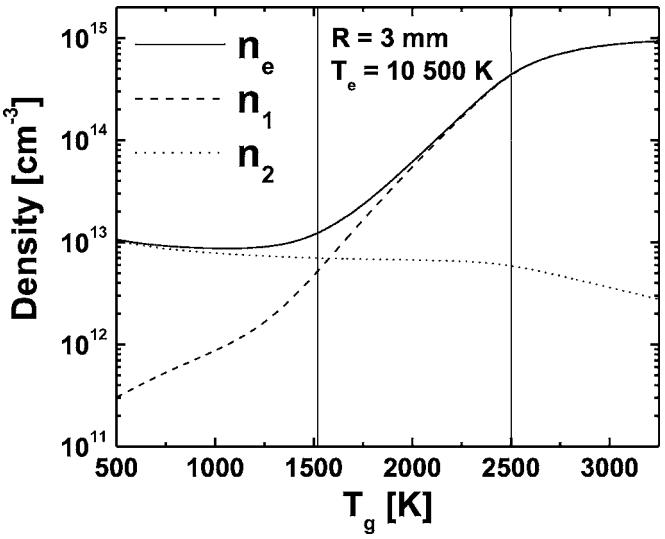

FIG. 16. Electron density n_e (full curve), atomic ion density n_1 (dashed curve), and molecular ion density n_2 (dotted curve) as functions of the gas temperature T_g at fixed value of the electron temperature T_e. After Ref. [9].

The left-hand side of Eq. (A1) accounts for ambipolar diffusion (D_{ae} being the ambipolar diffusion coefficient). The first term on the right-hand side represents direct ionization from the ground state, while the second one represents step ionization from metastable states (the $4s$ block). Charged-particle losses through dissociative recombination (rate coefficient ρ_{dr}) and three-body recombination (rate coefficient ρ_{tr}) are accounted for by the third and fourth terms, respectively. In Eq. (A1), the step ionization term results from two contributions: (i) step ionization through metastable states initially excited by electron collisions on the ground state and (ii) step ionization through metastable states populated by the process of dissociative recombination [28]. The coefficient η in Eq. (A1) accounts for the saturation of the step-ionization process at higher electron density. Expressions of the coefficients k_{si1} and k_{si2} are given by

$$k_{si1} = k_{0j} k_{ji} N \tau_j, \tag{A2}$$

$$k_{si2} = \rho_{dr} k_{ji} \tau_j, \tag{A3}$$

where τ_j is the characteristic time for the diffusion of metastable states. The rate coefficients k_{0j}, k_{ji} are defined in Table 1. While the contribution of the first term ($k_{si1} n_e^2$) to the process of step ionization is greater than the second one ($k_{si2} n_e^2 n_2$) at reduced pressure, the latter becomes dominant at atmospheric pressure because of the increasing contribution of dissociative recombination to the population of the metastable states. Note that the term $k_{si2} n_e^2 n_2$ is nonlinear with respect to the density of charged particles. When saturation of the step-ionization process occurs with increasing electron density ($\eta n_e \gg 1$), its ionization frequency nevertheless keeps depending on the density of MIs. As a result, any process affecting the density of MIs will affect the charged-particle creation process as well.

The dependence of the electron density on gas temperature is shown in Fig. 16, for argon sustained at atmospheric pressure with $T_e = 10\,500$ K. The dependence of atomic- and molecular-ion densities on T_g are also shown in Fig. 16. We observe that even though T_e is kept constant, n_e increases by almost two orders of magnitude when T_g varies between 1500 K and 3000 K. The density of AIs increases by more than three orders of magnitude, while the density of MIs decreases by almost an order of magnitude over the 500–3000 K gas temperature interval. The nonlinear increase of the electron density with T_g shown in Fig. 16 is induced by the strong (exponential) dependence of the process of MIs dissociation by atom-impact (rate coefficient k_3 in Table I) with T_g. Since MIs are more and more dissociated as T_g increases, there is a corresponding decrease in the charged-particle loss through dissociative recombination. The increase of n_e with T_g is further enhanced by the dissociation of MIs through electron-impact and the increasing contribution of the step-ionization process to the creation of charged particles, as the electron density increases.

[1] M. Moisan and Z. Zakrzewski, J. Phys. D **24**, 1025 (1991).

[2] *Microwave Discharges Fundamentals and Applications*, edited by C. M. Ferreira and M. Moisan,NATO ASI Series(Plenum, New York, 1992).

[3] M. Moisan and J. Pelletier, *Microwave Excited Plasmas* (Elsevier, New York, 1992).

[4] M. Moisan, J. Hubert, J. Margot, and Z. Zakrzewski, *Advanced Technologies Based on Wave and Beam Generated Plasmas* (Kluwer Academic, New York, 1999), p. 23.

[5] Yu. M. Aliev, H. Schlüter, and A. Shivarova, *Guided-Wave-Produced Plasmas* (Springer, Berlin, 2000).

[6] C. M. Ferreira and M. Moisan, Phys. Scr. **38**, 382 (1988).

[7] N. Djermanova, D. Grozev, K. Kirov, K. Makasheva, A. Shivarova, and Ts. Tsvetkov, J. Appl. Phys. **86**, 738 (1999).

[8] Y. Kabouzi, M. D. Calzada, M. Moisan, K. C. Tran, and C. Trassy, J. Appl. Phys. **91**, 1008 (2002).

[9] E. Castaños Martinez, Y. Kabouzi, K. Makasheva, and M. Moisan, Phys. Rev. E **70**, 066405 (2004).

[10] A. Yanguas-Gil, J. Cotrino, and A. R. Gonzàles-Elipe, Phys. Plasmas **11**, 5497 (2004).

[11] A. Sáinz, J. Margot, M. C. Garcia, and M. D. Calzada, J. Appl. Phys. **97**, 113305 (2005).

[12] Z. Zakrzewski, J. Phys. D **16**, 171 (1983).

[13] C. M. Ferreira, J. Phys. D **16**, 1673 (1983).

[14] M. Moisan and Z. Zakrzewski, Plasma Sources Sci. Technol. **4**, 379 (1995).

[15] H. Nowakowska, Z. Zakrzewski, M. Moisan, and M. Lubański, J. Phys. D **31**, 1422 (1998).

[16] H. Kousaka and K. Ono, Jpn. J. Appl. Phys., Part 1 **41**, 2199 (2002).

[17] H. Kousaka and K. Ono, Plasma Sources Sci. Technol. **12**, 273 (2003).

[18] G. J. M. Hagelaar and S. Villeger, IEEE Trans. Plasma Sci. **33**, 496 (2005).

[19] M. van den Donker, J. van Dijk, M. van Stralen, B. Broks, N. de Vries, G. Janssen, and J. van der Mullen, J. Phys. D **39**, 2553 (2006).

[20] M. A. Lieberman and A. J. Lichtenberg, *Principles of Plasma Discharges and Materials Processing* (Wiley, New York, 1994).

[21] U. Kortshagen, A. Shivarova, E. Tatarova, and D. Zamfirov, J. Phys. D **27**, 301 (1994).

[22] J. L. Delcroix and A. Bers, *Physique des Plasmas* (InterEditions, Paris, 1994).

[23] K. Makasheva and A. Shivarova, Phys. Plasmas **8**, 836 (2001).

[24] Yu. P. Raizer, *Gas Discharge Physics* (Springer, Berlin, 1991).

[25] A. J. Cunningham, T. F. O'Malley, and R. M. Hobson, J. Phys. B **14**, 773 (1981).

[26] E. W. McDaniel and E. A. Mason, *The Mobility and Diffusion of Ions in Gases* (Wiley, New York, 1973).

[27] J. D. C. Jones, D. J. Lister, D. P. Wareing, and N. D. Twiddy, J. Phys. B **13**, 3247 (1980).

[28] J. Jonkers, M. van de Sande, A. Sola, A. Gamero, A. Rodero, and J. van der Mullen, Plasma Sources Sci. Technol. **12**, 464 (2003).

[29] FEMLAB 3.0, www.comsol.com

[30] I. Ganashev, H. Sugai, S. Morita, and N. Toyoda, Plasma Sources Sci. Technol. **8**, 363 (1999).

[31] L. L. Alves, Eur. Phys. J.: Appl. Phys. **26**, 195 (2004).

[32] Yu. M. Aliev, J. Berndt, H. Schlüter, and A. Shivarova, Plasma Phys. Controlled Fusion **36**, 937 (1994).

[33] K. M. Green, M. C. Borràs, P. P. Woskov, G. J. Flores, K. Hadidi, and P. Thomas, IEEE Trans. Plasma Sci. **29**, 399 (2001).

[34] Y. Kabouzi, M. Moisan, J. C. Rostaing, C. Trassy, D. Guérin, D. Kéroack, and Z. Zakrzewski, J. Appl. Phys. **93**, 9483 (2003).

[35] M. Nantel-Valiquette, Y. Kabouzi, E. Castaños Martinez, K. Makasheva, M. Moisan, and J. C. Rostaing, Pure Appl. Chem. **78**, 1173 (2006).

[36] E. Castaños Martinez, Master's thesis, Université de Montréal, 2004.

[37] M. Moisan, J. Hubert, and R. Pantel, Contrib. Plasma Phys. **30**, 293 (1990).

[38] J. Berndt, D. Grozev, and H. Schlüter, J. Phys. D **33**, 877 (2000).

[39] Z. Rakem, P. Leprince, and J. Marec, J. Phys. D **25**, 953 (1992).

[40] M. Moisan and J. Pelletier, *Physique des Plasmas Collisionnels* (EDP Sciences, 2006).

[41] The term high-frequency refers to the radio-frequency domain and most of the microwave frequency domain, extending from 1 MHz to 40 GHz.

[42] The gas flow rate is calculated at room temperature and atmospheric pressure for comparison with experimental data.